



Structural and electrochemical properties of Cr-substituted lithium manganese oxide thin films

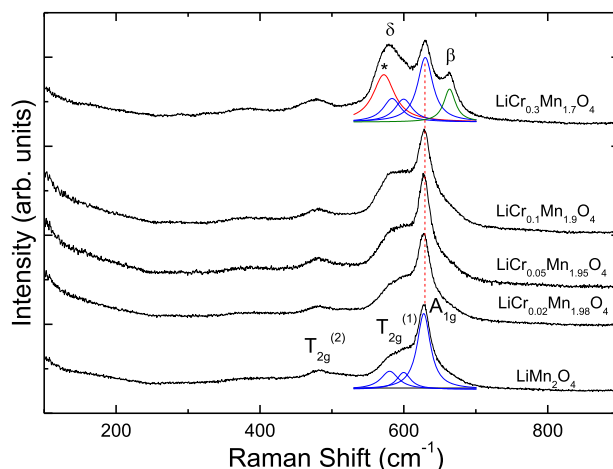
Kwang Joo Kim¹ · Jongho Park¹

Received: 19 November 2022 / Accepted: 2 April 2023 / Published online: 12 April 2023
© The Author(s), under exclusive licence to Springer Science+Business Media, LLC, part of Springer Nature 2023

Abstract

The advantages of Cr substitution in lithium manganese oxide (LiMn_2O_4) for cathode of rechargeable battery were investigated. $\text{LiCr}_x\text{Mn}_{2-x}\text{O}_4$ ($x \leq 0.3$) thin films were deposited on Pt/Ti/SiO₂/Si substrates via a sol-gel process. The $\text{LiCr}_x\text{Mn}_{2-x}\text{O}_4$ specimens were found to have the spinel structure of pristine LiMn_2O_4 with no detectable secondary phase. The Cr ions were found to be trivalent and to occupy the octahedral sites of the spinel lattice. The Cr-substituted specimens exhibited a new phonon mode near 570 cm^{-1} in the Raman spectrum. It is ascribed to octahedral $\text{Cr}^{3+}\text{-O}$ bonding (T_{2g}) that is located close to the mode due to octahedral $\text{Mn}^{3+}\text{-O}$ bonding (580 cm^{-1}). According to charge-discharge (C-D) cycling data on the $\text{LiCr}_x\text{Mn}_{2-x}\text{O}_4$ cathodes, the specimens of $x = 0.02$ and 0.05 kept larger capacities than that of the pristine LiMn_2O_4 cathode up to 700 cycles. The $x = 0.05$ cathode showed initial capacity close to that of $x = 0.02$. Above 100th cycle, the $x = 0.05$ cathode showed better capacity retention than that of $x = 0.02$. Possible reason for the improved capacity retention by the Cr substitution was discussed.

Graphical Abstract



Keywords Lithium manganese oxide · Thin film · Octahedral Cr^{3+} ion · Capacity retention · Rechargeable battery

✉ Kwang Joo Kim
kjkim@konkuk.ac.kr

¹ Department of Physics, Konkuk University, Seoul 05029, South Korea

Highlights

- $\text{LiCr}_x\text{Mn}_{2-x}\text{O}_4$ ($x \leq 0.3$) thin films were fabricated on Pt/Ti/SiO₂/Si substrates by using a sol–gel technique and post-annealing in air for 6 h at 700 °C.
- The $\text{LiCr}_x\text{Mn}_{2-x}\text{O}_4$ specimens were found to have the spinel structure of pristine LiMn_2O_4 with no detectable secondary phase.
- The Cr ions were found to be trivalent and to occupy the octahedral sites of the spinel lattice.
- A new phonon mode (δ) near 570 cm^{-1} observed in the Raman spectra of the Cr-substituted specimens confirms the octahedral Cr^{3+} occupation in the spinel lattice.
- The $\text{LiCr}_x\text{Mn}_{2-x}\text{O}_4$ cathodes with small Cr^{3+} compositions ($x < 0.1$) exhibited better capacity retention than the pristine LiMn_2O_4 cathode.

1 Introduction

Recently, rechargeable lithium batteries (RLBs) have been applied to heavy industries such as transportation vehicles and large-scale energy storage systems. The RLBs for such purposes need to be superb in energy density, thermal stability, and durability. Among the candidates for cathodes of such RLBs, LiMn_2O_4 and its derivatives have been under attention for their potential merits in charge capacity, operational safety and cost efficiency [1–3].

LiMn_2O_4 has cubic spinel structure where the tetrahedral (8a) and the octahedral (16d) sites are occupied by Li^+ and $\text{Mn}^{3+}/\text{Mn}^{4+}$ ions, respectively. The 8a and 16d sites are surrounded by four and six oxygen anions (O^{2-}) at the 32e sites, respectively. LiMn_2O_4 (LMO) cathode has theoretical charge capacity of 148 Ah kg^{-1} and effective cell potential of ~ 4.1 V vs. Li metal, leading to the energy density up to 304 Wh kg^{-1} . However, the practical charge capacity and the related energy density of the LMO cathode tend to be rather below the theoretical value [4].

During charging (Li^+ deintercalation) and discharging (Li^+ intercalation) in the LMO cathode, the Li^+ ions can migrate to the neighboring 8a sites via vacant octahedral 16c sites in the spinel lattice [5]. The inherent three-dimensional diffusion pathways in the spinel lattice of LMO need to facilitate Li^+ transport for ensuring charge capacity of the cathode. However, RLBs with the LMO cathodes have been reported to reveal rapid decay in charge capacity with repeated charge-discharge (C-D) cycle [3–6].

The capacity decay in LMO cathodes has been attributed to two reasons: decomposition and Jahn-Teller effect. Firstly, the decomposition of LMO cathode was found to be due to Mn dissolution in liquid electrolyte through the disproportionate reaction, $2\text{Mn}^{3+}(\text{solid}) \rightarrow \text{Mn}^{4+}(\text{solid}) + \text{Mn}^{2+}(\text{solution})$, at the cathode-electrolyte interface [7]. The resultant loss of cathode volume gives rise to a reduction in the charge capacity. Secondly, the Jahn-Teller distortion is caused by the appearance of high-spin $\text{Mn}^{3+}(t_g^3 e_g^1)$ ions at the octahedral sites during the discharging process [8–11], resulting in inefficient Li^+ insertion into the 8a sites that leads to a reduction in the charge capacity. There have been attempts to suppress the Mn

dissolution such as impurity substitution of other elements and surface coating of some metal oxides. With appropriate choice of the guest metal ions, the interactions between guest and host (Mn) ions of the LMO cathode can reinforce lattice energy to discourage the side reaction of the octahedral Mn^{3+} ions with liquid electrolyte [12].

In this investigation, structural and electrochemical properties of Cr-substituted LMO ($\text{LiCr}_x\text{Mn}_{2-x}\text{O}_4$) cathodes prepared as thin films using a sol–gel method are investigated in comparison with those of pristine LMO cathode. The thin-film cathodes ensure compositional uniformity that is necessary for reliable measurements of quantitative electrochemical parameters, while powder-based composite ones that are coated by conductive particles and binder are likely to face difficulty in measuring the intrinsic properties of the cathodic compound. Future development in micro-electronic devices that are operable with minimal current and power consumption will open the feasibility of thin-film microbatteries [13, 14] as power supplies. The sol–gel method has been reported to be advantageous over other techniques such as sputtering and spray deposition in fabricating the cathodes with high deposition rate, easy control of impurities, and low process cost.

The structural properties of the $\text{LiCr}_x\text{Mn}_{2-x}\text{O}_4$ cathodes were investigated through X-ray diffraction (XRD) for crystal structure, X-ray photoelectron spectroscopy (XPS) for the charge valence of the metal ions, and Raman spectroscopy for finding new lattice-vibrational modes in comparison with those of the LMO cathode. The electrochemical properties of the $\text{LiCr}_x\text{Mn}_{2-x}\text{O}_4$ cathodes were evaluated by measuring cyclic voltammetry (CV), C-D profile, and cycling performance in comparison with those of pristine LMO cathode.

2 Experimental

The $\text{LiCr}_x\text{Mn}_{2-x}\text{O}_4$ ($x \leq 0.3$) specimens were provided by using a sol–gel deposition method under the following sequence. (1) Preparation of precursor solution by dissolving manganese acetate tetrahydrate ($(\text{CH}_3\text{COO})_2\text{Mn} \cdot 4\text{H}_2\text{O}$), lithium acetate (CH_3COOLi), and chromium

nitrate nonahydrate ($\text{Cr}(\text{NO}_3)_3 \cdot 9\text{H}_2\text{O}$) powders together in a mixed solution composed of 25 ml of 2-methoxyethanol ($\text{CH}_3\text{O}(\text{CH}_2)_2\text{OH}$; 99%) and 2 ml of ethanolamine ($\text{NH}_2(\text{CH}_2)_2\text{OH}$; 99%) maintained at 200 °C. The weights of the ingredients of the specimens are listed in Table 1. (2) Spin-coating the solution on the substrate at 4000 rpm for 20 s followed by pre-heating at 300 °C for 5 min. After the gel formation, the spin-coating process was repeated to increase the film thickness. The $\text{LiCr}_x\text{Mn}_{2-x}\text{O}_4$ films were deposited on (111)-oriented Pt thin film with the thickness of 150 nm grown on multi-layered Ti/SiO₂/Si substrate. (3) Post-annealing in air for 6 h at 700 °C for transforming the gel into solid $\text{LiCr}_x\text{Mn}_{2-x}\text{O}_4$ film. The thicknesses of the $\text{LiCr}_x\text{Mn}_{2-x}\text{O}_4$ films measured from the side-view of their scanning-electron-microscopy images were close to 150 nm.

The crystal structure of the specimens was monitored by using XRD (Cu K α line, wavelength = 0.15418 nm) in the grazing-incidence geometry with fixed light incidence angle of 4° with the film plane. The diffraction data (2θ) were collected with a step width of 0.02°. The lattice-vibrational modes of the specimens were investigated by Raman scattering spectroscopy employing a diode laser (wavelength = 514 nm, power = 1 mW). The XPS measurements were performed using the Al K α line (photon energy = 1486.7 eV).

Electrochemical tests on the $\text{LiCr}_x\text{Mn}_{2-x}\text{O}_4$ cathodes were conducted on Li/LiCr_xMn_{2-x}O₄ cells [14] that were assembled in an argon-filled glove-box. The electrochemical cell consisted of a cathode, a metallic Li foil working as the reference electrode, and a porous membrane as the separator to isolate the cathode from the reference electrode. The cathode films had active area of ~1.0 cm². The liquid electrolyte for Li⁺ diffusion consisted of 1 M LiPF₆ dissolved in 1:1 vol% mixture of ethylene carbonate, (CH₂O)₂CO, and diethyl carbonate, (C₂H₅O)₂CO. In the C-D measurement at room temperature, the cell was electrochemically cycled in the 3.5–4.5 V potential range with a constant current density of 0.1 mA cm⁻², equivalent to ~10 C rate (corresponding to charge/discharge of 148 Ah kg⁻¹ in ~6 min) for 700 cycles. At all the C-D cut-off steps, the cell potential was potentiostated until the current decreased to 0.02 mA cm⁻². In the CV measurement at room temperature, the current density in the cell was measured with the cell potential scanned at 1.0 mV s⁻¹ between 3.5 and 4.5 V.

Table 1 Lists of wights of ingredients for $\text{LiCr}_x\text{Mn}_{2-x}\text{O}_4$ films

Cr composition	0.02	0.05	0.1	0.3
(CH ₃ COO) ₂ Mn·4H ₂ O	2.426 g	2.390 g	2.328 g	2.083 g
Cr(NO ₃) ₃ ·9H ₂ O	0.040 g	0.100 g	0.200 g	0.600 g
CH ₃ COOLi	0.351 g	0.351 g	0.351 g	0.351 g

3 Results and discussion

3.1 Structural properties

XRD patterns of the Cr-doped LMO films are exhibited in Fig. 1. All the indexed diffraction peaks in the patterns are coincident with those expected from cubic spinel structure (space group Fd $\bar{3}$ m). The XRD patterns show no secondary phase in the specimens. Also, the diffraction peaks are seen to hardly shift with increasing Cr composition (x) from those of LiMn_2O_4 (e.g., JCPDS 88-1030) as shown by dotted straight lines passing the (311), (400) and (440) peaks. The lattice parameters of the $\text{LiCr}_x\text{Mn}_{2-x}\text{O}_4$ specimens estimated by using a least-squares method were close to 0.822 nm.

In Fig. 2, Cr 2*p*-electron binding-energy (B-E) spectra of the $\text{LiCr}_x\text{Mn}_{2-x}\text{O}_4$ specimens obtained by the XPS measurements are exhibited. The electron B-E was calibrated by using the C 1*s* peak (254.8 eV) as a reference. The B-E spectrum consists of spin-orbit-split 2*p*_{3/2} and 2*p*_{1/2} peaks separated by ~10 eV (575.3 and 585.8 eV), implying the valence of the octahedral Cr ion to be +3. At higher B-E to the 2*p*_{3/2} peak another peak (α) appears at 576.3 eV. The shift of B-E can be explained in terms of a magnetic exchange interaction between a 2*p*_{3/2} hole and 3*d* electrons of the Cr³⁺ ion [15]. The absence of the (220) peak near $2\theta = 31^\circ$ in the XRD patterns of the Cr-doped specimens (Fig. 1) indicates that the Cr³⁺ ions mostly occupy the octahedral sites of the spinel lattice.

The vibrational modes of spinel $\text{LiCr}_x\text{Mn}_{2-x}\text{O}_4$ lattice structure were investigated by Raman scattering spectroscopy as shown in Fig. 3. Firstly, the strongest peak for the LMO specimen is located near 630 cm⁻¹ and such peak exists at the same energy for the $\text{LiCr}_x\text{Mn}_{2-x}\text{O}_4$ specimens. It has been assigned to A_{1g} phonon mode representing symmetric stretching vibration of O²⁻ ions at the tetrahedral sites

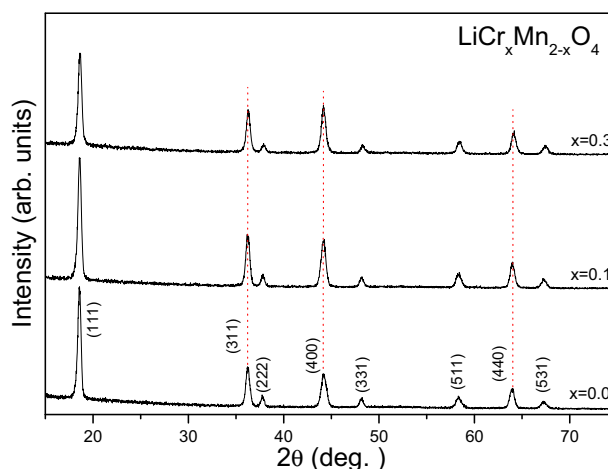


Fig. 1 XRD patterns of $\text{LiCr}_x\text{Mn}_{2-x}\text{O}_4$ cathodes in comparison with that of LiMn_2O_4 cathode

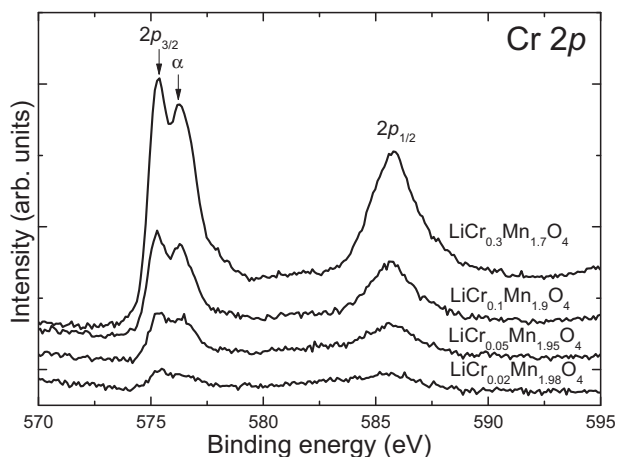


Fig. 2 Binding-energy spectrum of Cr 2*p* electron in $\text{LiCr}_x\text{Mn}_{2-x}\text{O}_4$ cathodes measured by XPS

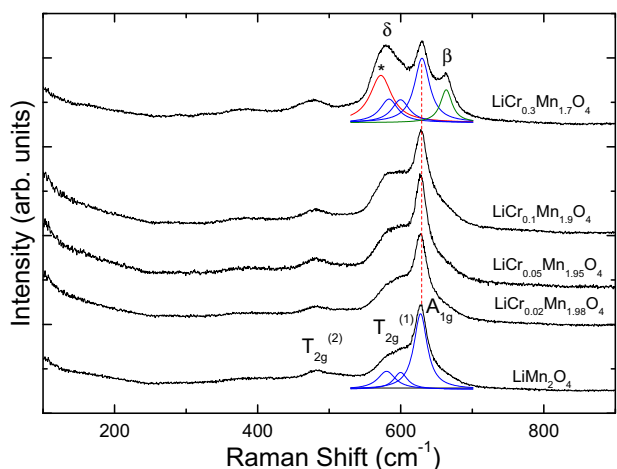


Fig. 3 Raman spectra of $\text{LiCr}_x\text{Mn}_{2-x}\text{O}_4$ cathodes in comparison with that of LiMn_2O_4 cathode

[11, 16, 17]. The fixed A_{1g} peak position for the Cr-substituted specimens to that of LMO supports the result of the XRD analyses indicating little change in the lattice parameter by the octahedral Cr^{3+} substitution. The peak (β) near 660 cm^{-1} is attributable to A_{2u} phonon mode representing asymmetric stretching vibration of O^{2-} ions at the tetrahedral sites. It is Raman-inactive for pristine LiMn_2O_4 but a breakdown in crystal symmetry due to the Cr^{3+} occupation in the spinel lattice is likely to make it Raman-active [11].

At the lower energies to the A_{1g} peak, two phonon peaks exist near 600 and 480 cm^{-1} for LMO. They have been assigned to $T_{2g}^{(1)}$ (600 cm^{-1}) and $T_{2g}^{(2)}$ (480 cm^{-1}) phonon modes representing Mn–O stretching vibrations of MnO_6 octahedron [16–18]. The broadened nature of the peaks compared to the A_{1g} peak is ascribed to the multivalence of the octahedral Mn ions, Mn^{3+} and Mn^{4+} (Mn^{4+} –O mode has higher energy than Mn^{3+} –O mode). As shown in Fig.

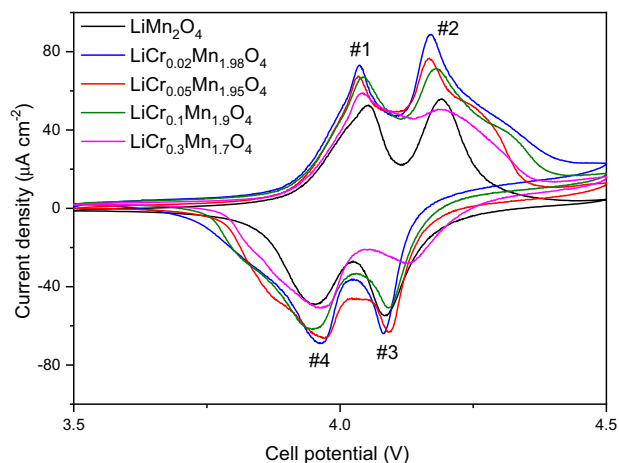


Fig. 4 CV curves of $\text{LiCr}_x\text{Mn}_{2-x}\text{O}_4$ cathodes in comparison with those of LiMn_2O_4 cathode

3, the $T_{2g}^{(1)}$ peak can be resolved to two lines at 600 cm^{-1} (Mn^{4+} –O) and 580 cm^{-1} (Mn^{3+} –O).

As the Cr composition increases, the $T_{2g}^{(1)}$ peak is seen to pick up strength. It is attributable to a new T_{2g} phonon mode near 570 cm^{-1} originating from Cr^{3+} –O stretching vibration of CrO_6 octahedron as denoted by δ [19]. The observed boosting of the mode δ implies the higher Raman scattering cross section of the octahedral Cr^{3+} –O bond compared to that of the Mn^{3+} –O bond [20]. The appearance of the Cr-related Raman-scattering peak for the $\text{LiCr}_x\text{Mn}_{2-x}\text{O}_4$ specimens supports the Cr^{3+} substitution in the octahedral sites of the spinel lattice.

3.2 Electrochemical properties

In Fig. 4, CV curves of the $\text{Li}/\text{LiCr}_x\text{Mn}_{2-x}\text{O}_4$ cells are compared with those of the LMO cell ($x = 0$). The CV patterns for the $x = 0.02, 0.05$ and 0.1 cathodes exhibit two well-refined peaks for both charging and discharging that are comparable to those of the LMO cathode. It indicates that the substituting Cr^{3+} ions do not alter the two binary equilibrium systems during the Li^+ extraction or insertion. The two-peak pattern of the current indicates that Li^+ extraction (charging) and the corresponding insertion (discharging) at the tetrahedral sites of the spinel lattice happen in two stages. For the Li^+ extraction, $\text{LiMn}_2\text{O}_4 \rightarrow \text{Li}_{0.5}\text{Mn}_2\text{O}_4$ (#1) and $\text{Li}_{0.5}\text{Mn}_2\text{O}_4 \rightarrow \text{Mn}_2\text{O}_4$ (#2) at the 8a sites associated with oxidation ($\text{Mn}^{3+} \rightarrow \text{Mn}^{4+}$), takes place with increasing cell potential, while for the Li^+ insertion, $\text{Mn}_2\text{O}_4 \rightarrow \text{Li}_{0.5}\text{Mn}_2\text{O}_4$ (#3) and $\text{Li}_{0.5}\text{Mn}_2\text{O}_4 \rightarrow \text{LiMn}_2\text{O}_4$ (#4) associated with reduction ($\text{Mn}^{4+} \rightarrow \text{Mn}^{3+}$), takes place with decreasing cell potential. For the LMO cathode, the current shows two peaks near 4.05 and 4.19 eV (separated by 140 meV) for charging and near 3.95 and 4.08 eV (separated by 130 meV) for discharging. It is notable that the strength of the two charge/discharge peaks is significantly reduced for $x = 0.3$, especially for the ones at the higher potential. It

implies a significant decrease in the cathode capacity that can be understood primarily in terms of a significant reduction in the quantity of oxidizable Mn^{3+} ions as the Cr^{3+} concentration increases. The area under a peak is likely to be proportional to Li^+ concentration involved in the stage. For the LMO cathode, the area of the two peaks are quite alike for both charging and discharging. However, for the Cr-substituted cathodes, the two peaks have different areas: except for $x = 0.3$, the peak at the higher (lower) potential has the larger area for charging (discharging). The dependence of the peak current density I_p (A cm^{-2}) on the potential scanning rate ν (V s^{-1}) can be applied to determine the diffusion coefficient D_{Li} of Li^+ ion on the basis of the following equation [21]:

$$I_p = (2.69 \times 10^5) n^{3/2} D_{\text{Li}}^{1/2} \nu^{1/2} C_{\text{Li}}$$

where n is the number of electrons per reaction species ($=1$ for Li^+) and C_{Li} is the bulk concentration of Li^+ ions in the electrode ($=0.02378 \text{ mol cm}^{-3}$ for LMO). Using the equation the value of D_{Li} (diffusion coefficient of Li^+) for Cr-substituted ($x = 0.02$) cathode from the peak #2 (charging, $I_p = 89 \times 10^{-6} \text{ A cm}^{-2}$) is calculated to be $1.9 \times 10^{-13} \text{ cm}^2 \text{ s}^{-1}$. It implies that a Li^+ ion moves 4.4 nm (equivalent to 5.4 lattice spacings of spinel LMO) in 1.0 s (diffusion length L in time t is $L = (D_{\text{Li}} t)^{1/2}$). On the other hand, from the peak #2 for the pristine LMO cathode (charging, $I_p = 56 \times 10^{-6} \text{ A cm}^{-2}$), $D_{\text{Li}} = 7.6 \times 10^{-14} \text{ cm}^2 \text{ s}^{-1}$, where a Li^+ ion moves 2.8 nm (equivalent to 3.4 lattice spacings of spinel LMO) in 1.0 s.

In Fig. 5a, b, and c, representative galvanostatic C-D curves of the Cr-substituted LMO cathodes are exhibited in comparison with those of pristine LMO cathode at the 1st, 200th, and 400th cycle, respectively. The charging and discharging curves reveal two plateaus corresponding to the two stages of Li^+ extraction and insertion mentioned for the CV patterns in Fig. 4. For the 1st cycle, the charge and discharge capacities of two Cr-substituted specimens ($x = 0.02$ and 0.05) are larger than those of the LMO specimen. The two Cr-substituted specimens also showed better C-D capacities at higher (200th and 400th) cycles than those of the LMO specimen. The coulombic efficiencies of the specimens at the 1st cycle were 95, 93, 97, 98, and 91% for the LMO, $x = 0.02$, $x = 0.05$, $x = 0.1$, and $x = 0.3$, respectively. At the later 200th (400th) cycles, they were 98% (96%), 98% (97%), 98% (98%), 99% (95%), and 94% (99%) for the LMO, $x = 0.02$, $x = 0.05$, $x = 0.1$, and $x = 0.3$, respectively. All the specimens are seen to exhibit good coulombic efficiencies at higher cycles as in the 1st cycle.

In Fig. 6, cycling performance (variation of discharge capacity with C-D cycles) curves of the $\text{Li}/\text{LiCr}_x\text{Mn}_{2-x}\text{O}_4$ cells are exhibited in comparison with that of LMO. The initial discharge capacity of the LMO cathode is 0.41 Ah cm^{-3} , equal to 64% of the theoretical capacity of 0.64 Ah cm^{-3} ($=148 \text{ Ah kg}^{-1}$) for spinel LiMn_2O_4 . For the $\text{LiCr}_x\text{Mn}_{2-x}\text{O}_4$ cathodes, the initial discharge capacities of the $x = 0.02$ and

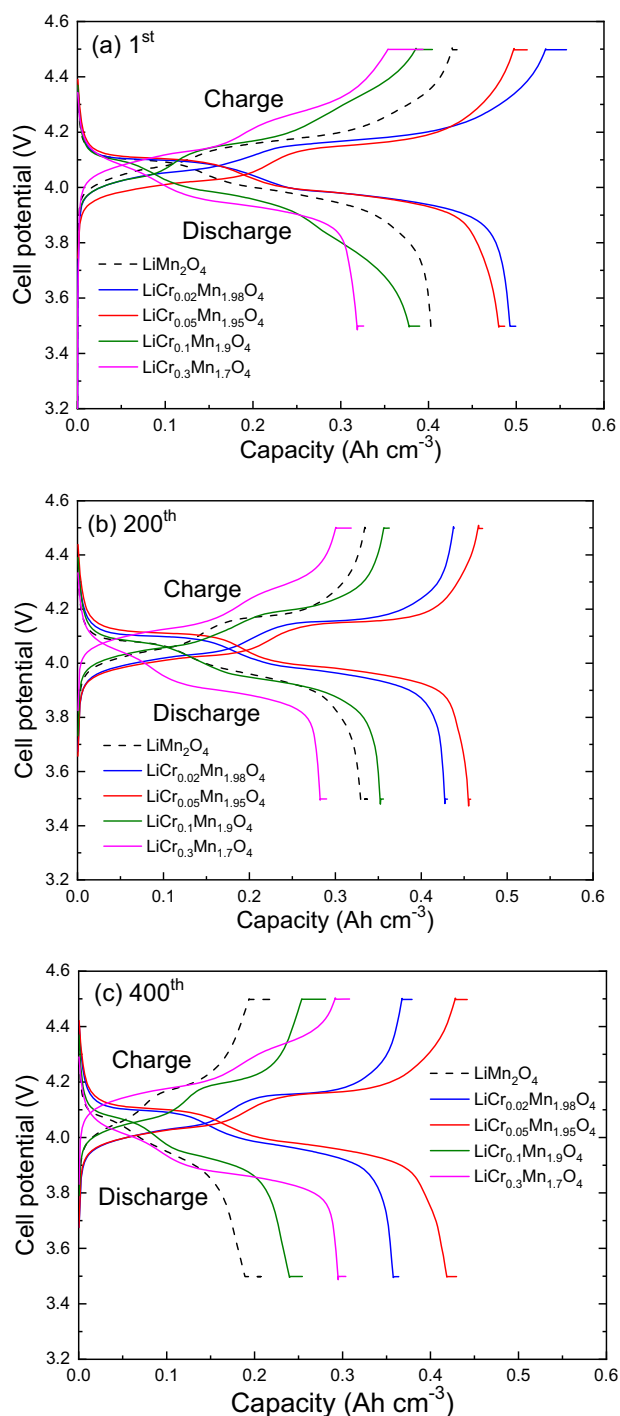


Fig. 5 Galvanostatic C-D curves of $\text{LiCr}_x\text{Mn}_{2-x}\text{O}_4$ cathodes at (a) 1st cycle, (b) 200th cycle, and (c) 400th cycle in comparison with those of LiMn_2O_4 cathode

0.05 cathodes are 0.50 and 0.49 Ah cm^{-3} , larger than that of pristine LMO cathode. On the other hand, it is 0.39 and 0.33 Ah cm^{-3} for the $x = 0.1$ and 0.3 cathode, respectively. Such a reduction in the initial capacity is primarily attributable to a reduction of octahedral Mn^{3+} population in $\text{LiCr}_x\text{Mn}_{2-x}\text{O}_4$ compared to LMO.

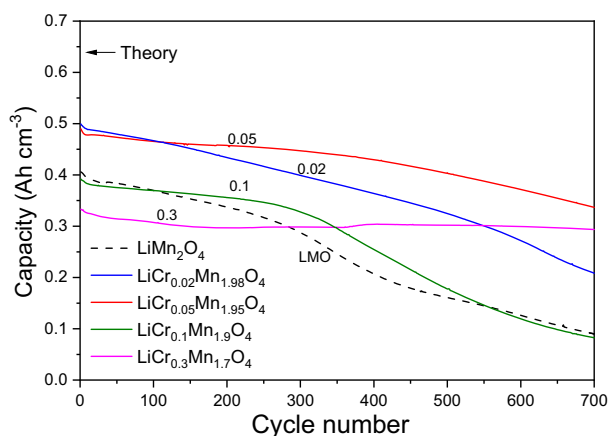


Fig. 6 Discharge capacities of $\text{LiCr}_x\text{Mn}_{2-x}\text{O}_4$ cathodes in comparison with that of LiMn_2O_4 cathode

It is notable that the $x = 0.02$ and 0.05 cathodes show better capacity retention capability than the LMO cathode for all the C-D cycles up to 700. For the $x = 0.02$ and 0.05 cathodes, the discharge capacity reaches to 0.40 Ah cm^{-3} (82% of its 1st cycle) and 0.45 Ah cm^{-3} (90% of its 1st cycle), respectively, at the 300th cycle. At the 700th cycle, they are reduced to 0.21 Ah cm^{-3} (42% of its 1st cycle) and 0.34 Ah cm^{-3} (69% of its 1st cycle) for $x = 0.02$ and 0.05 , respectively. For the LMO cathode, on the other hand, the capacity fading looks significant with increasing cycle: the discharge capacity reaches 0.29 Ah cm^{-3} (74% of its 1st cycle) at the 300th cycle and it is reduced to 0.09 Ah cm^{-3} (22% of its 1st cycle) at the 700th cycle. For the $x = 0.3$ cathode, the discharge capacity is maintained near $\sim 0.3 \text{ Ah cm}^{-3}$ (close to the initial discharge capacity) all the way to 700th cycle.

The galvanostatic C-D cycling data indicate that the octahedral Cr^{3+} substitution improve the capacity retention capability of the LMO cathode. The increase in the T_{2g} (δ) strength in the Raman spectrum of the Cr-substituted cathode (Fig. 3) implies the octahedral substitution of Cr^{3+} ions. The binding energy of octahedral Cr–O bonding in delithiated (CrO_2) state was estimated to be 1142 kJ mol^{-1} , being larger than that of Mn–O (946 kJ mol^{-1}) in $\alpha\text{-MnO}_2$ [22, 23]. Thus, the stronger Cr–O bonding is expected to be supportive for stabilizing the LMO-based spinel lattice. The improved capacity retention of the Cr-substituted LMO cathodes is primarily ascribed to the lattice stabilization through octahedral Cr–O bonding that can be effective for resisting to the Mn^{3+} dissolution at the cathode-electrolyte interface.

4 Conclusions

A series of $\text{LiCr}_x\text{Mn}_{2-x}\text{O}_4$ cathodes have been successfully fabricated as single-phased thin films on Pt(111)/Ti/SiO₂/Si substrates for rechargeable battery tests. The

XRD, XPS, and Raman data indicate that the Cr^{3+} ions mostly occupy the octahedral sites of the spinel lattice. The electrochemical cycling data for the $\text{LiCr}_x\text{Mn}_{2-x}\text{O}_4$ ($x = 0.02$ and 0.05) cathodes indicate a suppression of capacity deterioration compared to those of the LiMn_2O_4 cathode. The improved electrochemical properties of the $\text{LiCr}_x\text{Mn}_{2-x}\text{O}_4$ cathodes are explainable in terms of the appearance of octahedral Cr^{3+} –O bonds that boost structural stability for discouraging the disproportionate reaction of the Mn^{3+} ions.

Acknowledgements This research was supported by the Korea Basic Science Institute under the R&D program (Project No. D37700) supervised by the Ministry of Science and ICT.

Compliance with ethical standards

Conflict of interest The authors declare no competing interests.

References

- Xia Y, Ren X, Xiao Z, Gan Y, Zhang J, Huang H, He X, Mao Q, Wang G, Zhang W (2022) Spinel $\text{LiNi}_{0.5}\text{Mn}_{1.5}\text{O}_4$ shell enables Ni-rich layered oxide cathode with improved cycling stability and rate capability for high-energy lithium-ion batteries. *Electrochim Acta* 418:140352
- Su M, Chen Y, Liu H, Li J, Fu K, Zhou Y, Dou A, Liu Y (2022) Storage degradation mechanism of layered Ni-rich oxide cathode material $\text{LiNi}_{0.8}\text{Co}_{0.1}\text{Mn}_{0.1}\text{O}_2$. *Electrochim Acta* 422:140559
- Cen D, Kramer D, Monig R (2018) Chemomechanical fatigue of $\text{LiMn}_{1.95}\text{Al}_{0.05}\text{O}_4$ electrodes for lithium-ion batteries. *Electrochim Acta* 259:939
- Julien CM, Mauger A, Zaghbi K, Groult H (2014) Comparative issues of cathode materials for Li-ion batteries. *Inorganics* 2:132
- Liu D, Hamel-Paquet J, Trottier J, Barray F, Gariépy V, Hovington P, Guerfi A, Mauger A, Julien CM, Goodenough JB, Zaghbi K (2012) Synthesis of pure phase disordered $\text{LiMn}_{1.45}\text{Cr}_{0.1}\text{Ni}_{0.45}\text{O}_4$ by a post-annealing method. *J Power Sources* 217:400
- Qing C, Bai Y, Yang J, Zhang W (2011) Enhanced cycling stability of LiMn_2O_4 cathode by amorphous FePO_4 coating. *Electrochim Acta* 56:6612
- Xiong L, Xu Y, Tao T, Goodenough JB (2012) Synthesis and electrochemical characterization of multi-cations doped spinel LiMn_2O_4 used for lithium ion batteries. *J Power Sources* 199:214
- Yuan A, Tian L, Xu W, Wang Y (2010) Al-doped spinel $\text{LiAl}_{0.1}\text{Mn}_{1.9}\text{O}_4$ with improved high-rate cyclability in aqueous electrolyte. *J Power Sources* 195:5032
- Liu Z, Han K, Chen-Wiegart YK, Wang J, Kung HH, Wang J, Barnett SA, Faber KT (2017) X-ray nanotomography analysis of the microstructural evolution of LiMn_2O_4 electrodes. *J Power Sources* 360:460
- Mikhailova D, Thomas A, Oswald S, Gruner W, Bramnik NN, Tsirlin AA, Trots DM, Senyshyn A, Eckert J, Ehrenberg H (2013) Structural changes in the LiCrMnO_4 cathode material during electrochemical Li extraction and insertion. *J Electrochem Soc* 160:A3082
- Molenda M, Dziembaj R, Podstawka E, Proniewicz LM (2005) Changes in local structure of lithium manganese spinels ($\text{Li}:\text{Mn} = 1:2$) characterised by XRD, DSC, TGA, IR, and Raman spectroscopy. *J Phys Chem Solids* 66:1761

12. Xiao L, Zhao Y, Yang Y, Cao Y, Ai X, Yang H (2008) Enhanced electrochemical stability of Al-doped LiMn_2O_4 synthesized by a polymer-pyrolysis method. *Electrochim Acta* 54:545
13. Larfaillou S, Guy-Bouyssou D, Cras F, Franger S (2016) Comprehensive characterization of all-solid-state thin films commercial microbatteries by electrochemical impedance spectroscopy. *J Power Sources* 319:139
14. Lee JH, Kim KJ (2013) Superior electrochemical properties of Mn_2O_3 -coated LiMn_2O_4 thin-film cathodes for Li-ion microbatteries. *Electrochim Acta* 102:196
15. Shkvarin AS, Yarmoshenko YM, Yablonskikh MV, Skorikov NA, Merentsov AI, Kuznetsov MV, Titov AN (2012) MxTiSe_2 ($M = \text{Cr, Mn, Cu}$) electronic structure study by methods of resonance X-ray photoemission spectroscopy and X-ray absorption spectroscopy. *J Phys Chem Solids* 73:1562
16. Amundsen B, Burns GR, Islam MS, Kanoh H, Roziere J (1999) Lattice dynamics and vibrational spectra of lithium manganese oxides: A computer simulation and spectroscopic study. *J Phys Chem B* 103:5175
17. Julien CM, Massot M (2003) Lattice vibrations of materials for lithium rechargeable batteries I. Lithium manganese oxide spinel. *Mater Sci Eng B* 97:217
18. Kopec M, Dygaa JR, Krok F, Mauger A, Gendron AF, Julien CM (2008) Magnetic characterization of $\text{Li}_{1+x}\text{Mn}_{2-x}\text{O}_4$ spinel ($0 \leq x \leq 1/3$). *J Phys Chem Solids* 69:955
19. Hwang S-J, Park D-H, Choy J-H, Campet G (2004) Effect of chromium substitution on the lattice vibration of spinel lithium manganate: A new interpretation of Raman spectrum of LiMn_2O_4 . *J Phys Chem B* 108:12713
20. Strobel P, Ibarra-Palos A, Anne M, Poinsignon C, Crisci A (2003) Cation ordering in $\text{Li}_2\text{Mn}_3\text{MO}_8$ spinels: structural and vibration spectroscopy studies. *Solid State Sci* 5:1009
21. Cheng F, Wang H, Zhu Z, Wang Y, Zhang T, Tao Z, Chen J (2011) Porous LiMn_2O_4 nanorods with durable high-rate capability for rechargeable Li-ion batteries. *Energy Environ Sci* 4:3668
22. Wei Y, Kim K-B, Chen G (2006) Evolution of the local structure and electrochemical properties of spinel $\text{LiNi}_x\text{Mn}_{2-x}\text{O}_4$ ($0 \leq x \leq 0.5$). *Electrochim Acta* 51:3365
23. Thirunakaran R, Kim KT, Kang YM, Seo CY, Lee JY (2004) Adipic acid assisted sol-gel route for synthesis of $\text{LiCr}_x\text{Mn}_{2-x}\text{O}_4$ cathode material. *J Power Sources* 137:100

Publisher's note Springer Nature remains neutral with regard to jurisdictional claims in published maps and institutional affiliations.

Springer Nature or its licensor (e.g. a society or other partner) holds exclusive rights to this article under a publishing agreement with the author(s) or other rightsholder(s); author self-archiving of the accepted manuscript version of this article is solely governed by the terms of such publishing agreement and applicable law.